ELSEVIER

Journal of Hazardous Materials 44 (1995) 185–207

JOURNAL OF HAZARDOUS MATERIALS

Modeling and validation of a dispersing aerosol jet

John L. Woodward[a,*], Julian Cook[b], Antonis Papadourakis[c]

[a]*DNV Technica Inc., 355 E. Campus View Blvd., Suite 170, Columbus, OH 43235, USA*
[b]*DNV Technica Ltd., Palace House, 3 Cathedral Street, London, SE1 9DE, UK*
[c]*Rohm and Haas Co., P.O. Box 584, Bristol, PA 19007, USA*

Received 10 September 1994; accepted 7 April 1995

Abstract

A fundamental model has been developed to simulate the dispersion and trajectories of a high-momentum aerosol jet. The model predicts droplet evaporation or condensation rates based on heat and mass transfer correlations and on the vapor backpressure or concentration in the plume. Modeling details are provided here along with a practical strategy for tuning the several modules. This approach makes use of decoupled experiments and avoids iterative loops. The rainout fraction predicted by this model is a sensitive function of the initial drop size.

Keywords: Dispersion modeling; Two-phase aerosol; Model validation; Drop evaporation

1. Introduction

A greater hazard is generally posed by accidental discharges of toxic or flammable materials as pressurized liquids than as gases or vapors. This is because pressurized liquids tend to form an aerosol cloud which has considerably greater density and thus source strength than vapor or gas clouds. It is important to be able to predict the mass fraction of liquid which evaporates or remains suspended as aerosol droplets, or, conversely, the fraction which rains out. The rained out fraction will form a pool on the ground or on water and subsequently reevaporate or partially dissolve in the water. Rainout generally results in weakening the original cloud but extending the duration of the hazardous event because of evaporation of the rained out liquid.

In experiments sponsored by the Center for Chemical Process Safety (CCPS) of the American Institute of Chemical Engineers (AIChE), measurements were made of the fraction of liquid captured after rainout from aerosol discharges [1–3]. With the limitations of the experimental method, it was not possible to measure all of the phenomena occurring, in particular, evaporation within the plume and reevaporation

* Corresponding author.

SSDI 0304-3894(95)00054-2

of the rained out liquid. In order to maximize the utility of these experiments, we wish to apply modeling to provide a consistent basis for predicting the unmeasured phenomena. The basis for such modeling must be provided by other, independent experiments. We discuss here this basis by showing how the various modeling modules which make up an integrated model of aerosol dispersion have been tuned to experimental data. In an accompanying paper [4], we discuss how this model was used to reassess the CCPS rainout data and to develop correlations for drop size.
An integrated model must predict the following:
- discharge rate,
- aerosol flash fraction and Sauter mean drop diameters,
- jet entrainment and trajectories, particularly to touchdown,
- droplet evaporation in the plume,
- rainout,
- pool spread and evaporation,
- dissolution of soluble material spilled on water,
- dilution of vapors across the pool surface,
- heavy gas dispersion,
- passive dispersion.

We have developed a model that integrates the above prediction modules, called the unified dispersion model (UDM). We concentrate here on the modules for jet entrainment, jet and drop trajectories, and rainout. Pool spread and evaporation is treated in an appendix, with a brief treatment of dissolution of soluble material. Other modules have been documented elsewhere [5].

2. Model overview

After starting with calculation of discharge rate and aerosol flash fraction, the UDM describes the physical phenomena illustrated in Fig. 1. An elevated, heavy vapour/aerosol release is modeled as a circular cross section which tends to flatten into an ellipse as the cloud settles. Upon touching down, the cross section becomes a truncated ellipse, and the cloud levels off as the vertical component of momentum is dissipated. Aerosol droplets may rain out shortly after touchdown. Rainout produces a pool which spreads and vaporizes. The vapor from the pool is added back to the plume, as a function of time. The plume may become buoyant and lift off and rise until constrained by the mixing layer.

A module for modeling droplet evaporation for an aerosol jet combined with entrainment and plume trajectory prediction has been previously documented [6, 7]. This model uses nonequilibrium heat and mass transfer correlations, and typically the liquid temperature decreases below the vapor temperature. Since evaporation then takes place at a lower vapor pressure, larger mass fractions rain out than are predicted by models which assume that thermal equilibrium is achieved with entrained air.

In subsequent developments, the jet dispersion module has been improved [8, 9] to provide a smoother model of touchdown and liftoff, and concentration profiles which become more diffuse farther downwind. The two sets of differential equations

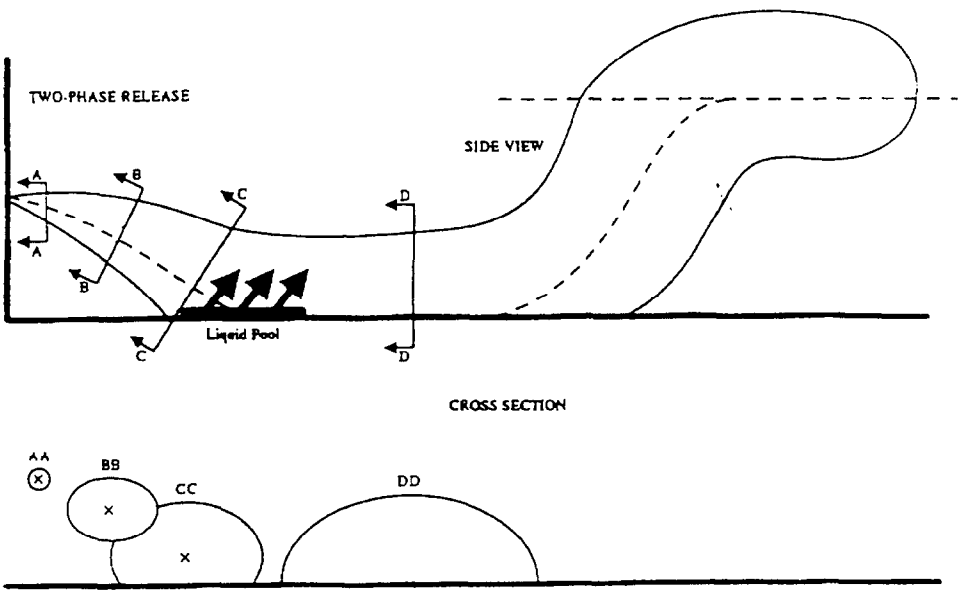

Fig. 1. Idealized cloud section: side and cross-sectional views of a two-phase, elevated continuous release at various stages of dispersion.

(for drops and jet) are integrated separately by a Runge–Kutta–Milne (RKM) integration scheme. For stability, the step size of the drop evaporation integration is constrained not only by the RKM error criterion but also by requiring liquid temperature changes to be no larger than 2.5%. The two integrations are kept synchronized in the horizontal direction.

The rained out liquid is then modeled as a spreading, circular pool until it reaches the bund walls, or until it reaches a steady-state pool size in which the rate of evaporation and dissolution matches the rate of inflow of mass to the pool.

3. Cloud dispersion model

Over a wide range from the near field to the far field, the dispersion mechanisms affecting a dispersing cloud vary, so the differential equation for mass transfer, in general is:

Conservation of species (air entrainment):

$$\frac{dm_{cld}}{ds} = \text{logic selects between } E_{jet}, E_{hvy}, E_{pas}, \tag{1}$$

where E_{jet}, E_{hvy} and E_{pas} are, respectively the jet, heavy gas and passive mass entrainment rates. Both continuous and instantaneous releases are treated by appropriately changing between spatial and time derivatives. We show here the continuous discharge solution.

In the near field, the high-momentum jet mechanism dominates after a high-pressure release, as given by

$$E_{\text{jet}} = \alpha_1 [m_{\text{cld}} \rho_{\text{air}} | u_0 - u_w \cos\theta |]^{1/2} + \alpha_2 \rho_{\text{air}} P_{\text{abov}} | u_w \sin\theta |. \tag{2}$$

During the jet dispersion phase, the centerline velocity decays until either the heavy gas or the passive dispersion mechanisms become dominant. For a low-momentum release, the jet dispersion mode may never be dominant. The entrainment rates for the heavy-gas, and the passive regimes are described elsewhere [9]. The other differential equations describing momentum, position, and energy follow.

Conservation of excess horizontal component of momentum:

$$\frac{dI_{x2}}{ds} = C_{\text{Dj}} P_{\text{abov}} \rho_{\text{cld}} (u_w \sin\theta)^2 |\sin\theta| + C_{\text{Dgnd}} P_{\text{abov}} \rho_{\text{cld}} (u_w - u_x). \tag{3}$$

It is advantageous to model excess momentum, obtained by subtracting the term which increases indefinitely ($u_w m_{\text{cld}}$). This excess momentum decays to zero in the far field, and is easier to treat. The second term is added only when the cloud is touching the ground, and ($u_w - u_x$) is greater than a threshold value. P_{abov} is the perimeter of the nominal elliptical cross section of the cloud above the ground.

Conservation of vertical component of momentum:

$$\frac{dI_z}{ds} = -\frac{m_{\text{cld}}}{\rho_{\text{cld}}} (\rho_{\text{cld}} - \rho_{\text{air}}) g - C_{\text{Dj}} P_{\text{abov}} \rho_{\text{cld}} (u_w \sin\theta)^2 |\cos\theta| \frac{\sin\theta}{|\sin\theta|}. \tag{4}$$

Vertical momentum increases by the buoyancy term and is decreased by the plume drag term.

Horizontal and vertical centerline position:

$$\frac{1}{u_0}\frac{dx}{dt} = \frac{dx}{ds} = \cos\theta, \qquad \frac{1}{u_0}\frac{dz}{dt} = \frac{dz}{ds} = \sin\theta. \tag{5}$$

The rate of heat convection from the substrate is

$$u_0 \frac{dq_{\text{GND}}}{ds} = \max(q_{\text{N}}, q_{\text{F}}) S. \tag{6}$$

For continuous releases S is the width of the cloud in contact with the ground. For instantaneous releases, S is the contacting area of the cloud. Both natural and forced convection are modeled, given respectively, by q_{N} and q_{F}, as described in Cook and Woodward [8].

Additional equations describe momentum conservation upon touchdown [9]. Momentum is conserved at touchdown by increasing both the x and y direction momentum (forward velocity and spread rate) to match the decrease in vertical momentum which goes to zero. As the vertical momentum goes to zero, the vector for cloud direction becomes horizontal. Incidentally, for a buoyant cloud lifting off, this situation is reversed. Upon developing a positive value of vertical momentum, the vector for cloud direction points more and more upwards. The cloud cross-sectional ellipse remains truncated until the bottom edge of the ellipse rises above the ground.

4. Cloud profiles and geometry

The profile form assumed here was suggested by Webber et al. [10]. The concentration profile is given by

$$c(x,y,z) = \begin{cases} c_0(x)F_v(z)F_h(y)F_h(x) & \text{(inst)}, \\ c_0(x)F_v(z)F_h(y) & \text{(cont)}, \end{cases} \tag{7}$$

$$F_v(z) = \exp\left[-\left(\frac{z}{a_3(x)}\right)^s \right], \qquad F_h(y) = \exp\left[-\left(\frac{y}{a_2(x)}\right)^m \right],$$

$$F_h(x) = \exp\left[-\left(\frac{x - x_0}{a_2(x)}\right)^m \right] \tag{8}$$

where x_0 is the position of the center of the cloud.

The scaling coefficients in Eq. (8) are:

$$a_2 = \lambda, \quad W = \lambda\sqrt{2}\sigma_y, \qquad a_3 = \lambda, \quad R = \lambda\sqrt{2}\sigma_z, \tag{9}$$

where the Schmidt number λ scales velocity profiles to concentration and density profiles ($\lambda^2 = 1.4$), and σ_y and σ_z are the standard deviations.

Eq. (8) reduces to the Gaussian form when $s = m = 2$. For larger values, say $m = 50$, profiles are predicted by Eq. (8) to be very nearly sharp-edged. This formulation allows modeling of a sharp-edged jet, as occurs from a smooth-edged nozzle, dispersing to a jet with a more nearly Gaussian profile farther downwind. The exponent m is correlated as a function of the normalized density difference which goes into the calculation of buoyancy. The correlation for s is similar to the correlations for atmospheric flux gradients.

The effective height of the plume is defined by

$$H = \frac{1}{c_0}\int_0^\infty c\,\mathrm{d}z = \Gamma\left(1 + \frac{1}{s}\right)a_3(x). \tag{10}$$

Similarly, the effective half-width of the cloud is given by

$$W = \frac{1}{c_0}\int_0^\infty c(x,y)\,\mathrm{d}y = \begin{cases} \Gamma\left(1 + \dfrac{1}{m}\right)a_2(x) & \text{(inst)}, \\ \left[\dfrac{\pi}{4}\Gamma\left(1 + \dfrac{2}{m}\right)\right]^{1/2} a_2(x) & \text{(cont)}. \end{cases} \tag{11}$$

The physical interpretation of the effective width and length is that the concentration profiles are squared off, so the dimensions H and W define an ellipse-shaped cross section of a top hat model which contains all the mass in the cloud having the diffuse concentration profile given by Eqs. (7) and (8). This general similarity model, therefore, retains all the simplicity and convenience of a top hat model, but at the same time allows quite general concentration profiles. A further simplification is to retain the

elliptical cloud cross section as the cloud position changes from elevated to touching down to grounded. Only that portion of the cross section which is above ground is physical (contains aerosol or vapor).

5. Droplet evaporation model

An aerosol is considered to consist of single-sized spherical droplets surrounded by a mixture of air and evaporated vapor. The concentration in the plume provides the backpressure which decreases the driving force for mass transfer. Standard drag correlations are used to allow the plume velocities to affect the drop trajectories. Stokes law laminar-flow settling velocities are invoked as a lower limit when other drag forces decay. The following system of ordinary differential equations is integrated to obtain the liquid mass, temperature, and position, written for a continuous release.

Mass balance by evaporation or condensation:

$$u_d \frac{dm_d}{ds} = -A_d K_g \rho_c(T_g) C' \ln\left[\frac{1-y_g}{1-\frac{y_s}{T_d/T_g}}\right]. \tag{12}$$

Energy balance by heat conduction, radiation, and evaporation or condensation:

$$u_d \frac{dT_d}{ds} = \frac{A_d h(T_g - T_d) + \frac{dm_d}{dt} h_{fg} + A_d \sigma_r \varepsilon (T_{alm}^4 - T_d^4)}{(m_d C_{pL})}. \tag{13}$$

Force balance for vertical component of drop momentum (for $dm_d/dt < 0$):

$$u_d \frac{dI_{dz}}{ds} = -u_{dz}\left(\frac{dm_d}{dt}\right) + \frac{m_d}{\rho_L}(\rho_g - \rho_L)g + C_D \frac{1}{2} \rho_g u_{dgz} |u_{dg}| \pi r_d^2. \tag{14}$$

Horizontal and vertical droplet position:

$$\frac{dx_d}{ds} = \frac{u_x}{u_d} = \cos\theta_d, \quad \frac{dz_d}{ds} = \frac{u_z}{u_d} = \sin\theta_d. \tag{15}$$

The first term in Eq. (14) represents the droplet jet effect of evaporation enhancing momentum in the direction indicated by u_{dz}, the vertical droplet velocity. The correlation chosen for heat and mass transfer to and from the drops is a hybrid of the correlations of Fuchs [11] and of Eisenklam et al. [12]. We favor the more recent form of the heat and mass transfer correlation which makes use of the transfer number, B_m proposed by Eisenklam et al. for fuel droplets injected into a burner, in which a very wide range of temperatures is considered.

The mass transfer coefficient in Eq. (12) and the heat transfer coefficient in Eq. (13) are found from the Sherwood number and Nusselt number correlations:

$$K_g = Sh\, D_{12}/r_d, \tag{16}$$

$$h = Nu\, k/r_d. \tag{17}$$

$$Sh = (a + b Re^{1/2} Sc^{1/3})/(1 + B_m), \tag{18}$$

$$Nu = (a + b Re^{1/2} Pr^{1/3})/(1 + B_m). \tag{19}$$

For the thermal conductivity, k, and diffusivities, we use, respectively, the physical properties correlations of the AIChE DIPPR system (Design Institute of Physical Properties Research) and the method of Wilke and Lee as given in Reid et al. [13].

The correction constant C' in Eq. (12) is made up of two terms, a term for Stefan flow which accounts for enhanced evaporation at high mass flux, and a correction for the temperature gradient on the diffusion coefficient as described by Barrett and Clement [14].

$$C' = C_s \cdot C_T, \tag{20}$$

$$C_s = 1 + \frac{P_{sat} + y_g P_a}{2P_a}, \tag{21}$$

$$C_t = \frac{(2 - \mu)(T_g - T_L)}{T_g^{\mu - 1}(T_g^{2-\mu} - T_L^{2-\mu})}, \tag{22}$$

where μ varies with composition, but in most cases [15]:

$$1.6 < \mu < 2,$$

so we used $\mu = 1.8$.

The horizontal component of drop velocity is set equal to the horizontal component of the jet. This is consistent with treating the momentum of the plume to include the momentum of the drops. The drop position is found by integrating the horizontal and vertical components of drop velocity. Drops are allowed to fall outside the plume boundaries, in which case the backpressure affecting the mass transfer driving force drops to zero. Vapor evaporating from the drops is added to the plume. Upon rainout, the mass, momentum, and enthalpy of the rained-out liquid is subtracted from the plume.

This treatment is a nonequilibrium approach, since the drop temperature is determined through an unsteady-state energy balance rather than through a flash calculation. Typically, the drop temperature falls below the gas temperature. For some discharge conditions, the driving force for evaporation becomes negative so that condensation occurs. When the driving force approaches zero the nonequilibrium model's predictions approach those of the equilibrium model.

6. Module tuning procedure makes use of decoupling

Fortunately, a high degree of decoupling of the modeling modules can be obtained, or the task would be quite imposing. A number of experiments have been designed to independently verify a single module or modeled variable. Essentially decoupled experiments should be used to first obtain or verify the following modules:

– Discharge rate predictions are made by numerically maximizing the mass flux along an isentropic path using the energy balance equation. These predictions can be verified by discharge rate measurements, and no tuning constants need to be adjusted, as discussed by Woodward [16, 17].

– A fairly large body of data has been developed using dilute concentrations of a tracer gas, for example, the Hanford Continuous, and Prairy Grass test series. These data, applicable to the passive dispersion regime, have been used to develop standard passive dispersion correlations for the concentration standard deviations, σ_{ya} and σ_{za} as a function of downwind distance, x and of surface roughness length, z_0. We used the correlations of McMullen [18] and Hosker [19].

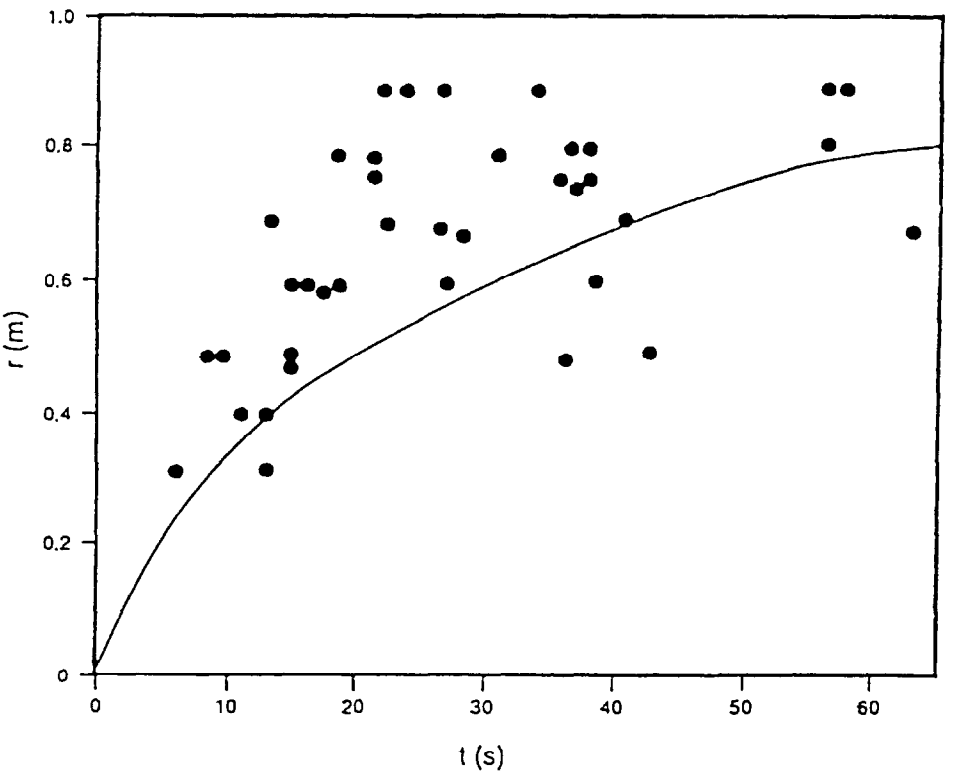

Fig. 2. Comparison of pool spread rate predictions with experimental data for water spreading continuously on plywood: Experimental data from Run 28 of Belore and McBean [32].

Decoupled tuning can be accomplished by selecting in succession experiments which largely isolate the phenomenon of interest. For example:
– Although coupled for volatile materials, pool spread and vaporization can be decoupled by first using experiments with nonvolatile materials to set the constants governing spread rate. This has been reported by Woodward [20], Cook and Woodward [8] and in our model theory notes [5, 21]. The only adjustable parameter for spread on a solid substrate is the minimum pool thickness, h_{min}, for which we use a value of 2 mm for smooth surfaces, and up to 5 mm for rough surfaces. An example comparison with data for water spread rates on plywood is shown in Fig. 2. The data scatter for these particular experiments is large. Fig. 3 compares spread rate data for kerosene spilled instantaneously on water, illustrating two spread rate regimes in the modeling module. The constants found by Dodge et al. [22] for liquid spreading on water are used unaltered.

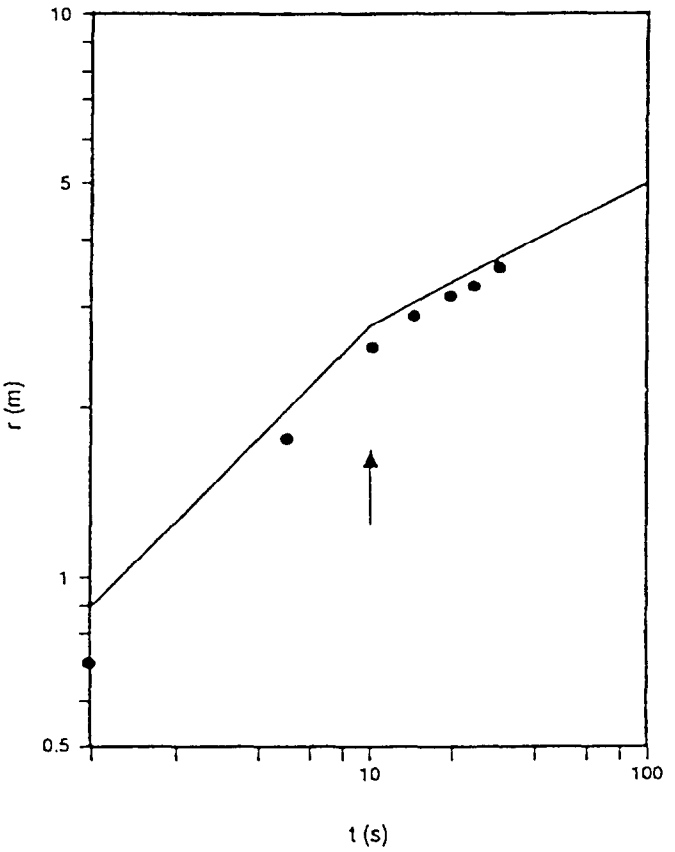

Fig. 3. Comparison of pool spread rate predictions with experimental data for an instantaneous spill of kerosene on water: Experimental data from Dodge et al. [22] for 31.8 kg of kerosene spilled on water. The change in slope at about 10 s indicates a transition from the gravity–inertial regime to the gravity-viscous regime.

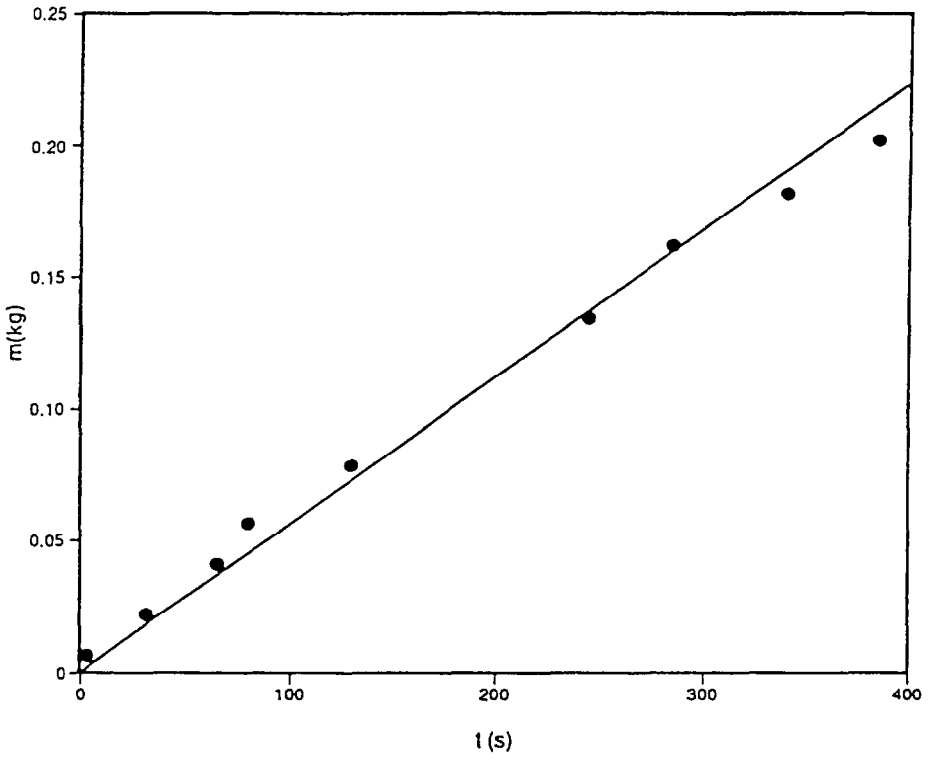

Fig. 4. Comparison of predictions of total mass evaporated with experimental data for an instantaneous spill of butane on a confined water surface: Experimental data by Reid and Smith [33, 34].

– The constants governing evaporation rates from a pool are set using experiments with stationary evaporating pools such as MacKay and Matsugu [23], Kawamura and MacKay [24], and Norman and Dowell [25]. This gives 0.0021 in Eq. (A.13) in the Appendix, the mass transfer rate correlation. All other constants in the heat transfer terms are taken from standard correlations without adjustment. Experimental spills of volatile materials confirm that the constants found this way apply well when both spreading and vaporization occur simultaneously. For example, Fig. 4 compares model predictions with evaporation rate data for butane spilled instantaneously on water in a confined area.

– Use experiments with spills of water-soluble materials to set the constants involving dissolution rate. We used the data sets developed by Dodge et al. [22] as discussed in our model theory notes [5, 21].

Tuning of two of the three dispersion regime modules, the heavy-gas module and the passive regime module, is dicussed elsewhere [26]. We focus here on tuning the high-momentum jet module. An advantageous property of our formulation of the jet module is that the tuning constants are readily set by the following sequence:

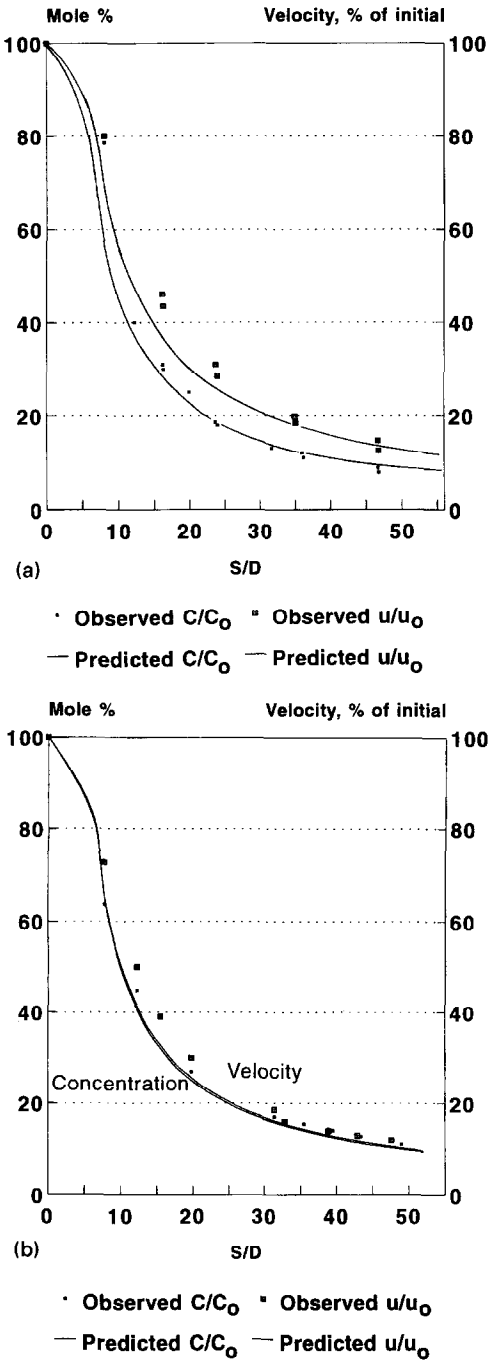

Fig. 5. Comparison of model predictions for centerline concentration and centerline velocity of a gas jet of (A) CO_2, (B) Nitrogen, (C) Helium. Experimental data by Keagy and Weller [27] for jet at 121 m s^{-1} into still air.

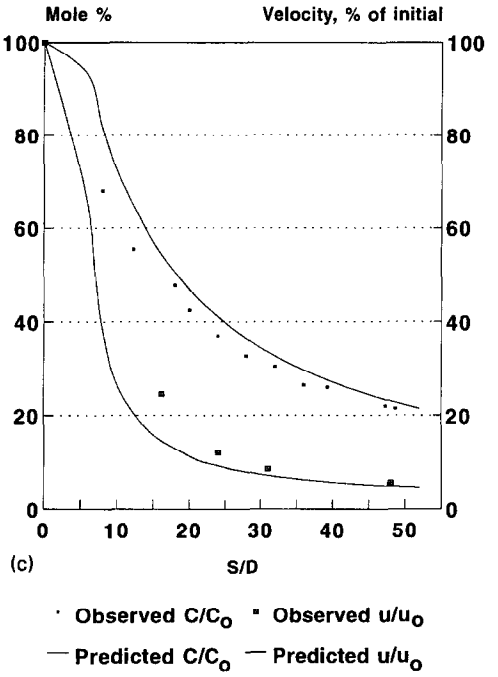

Fig. 5. Continued.

– First use jet experiments into still air to set $\alpha_1 = 0.16$ in Eq. (2). Both centerline concentration and velocity fit the data by setting this single parameter. For example, Figs. 5(A)–(C) compare model predictions for the data of Keagy and Weller [27] for carbon dioxide, nitrogen, and helium.
– Second use centerline concentration data for jets in a cross wind to set $\alpha_2 = 0.29$ in Eq. (2). This constant affects air entrainment rate, and thereby the plume momentum by conservation of momentum. Fig. 6 compares the data of Birch as cited by Cleaver and Edwards [28] with model predictions.
– Third, set $C_{Dj} = 0.15$ in Eq. (3) to match centerline trajectory profiles for jets in a cross wind. An extensive set of data are available for such plume trajectories. Fig. 7 shows how the UDM profiles compare with the average of a number of data sets as summarized by Rajaratnam [29] consistent also with data by Keffer and Baines [30]. Similarly, the droplet evaporation and trajectory model can be tuned by sequentially using decoupled experiments.
– First use experiments for the evaporation of a single drop in still air such as the data of Ranz and Marshall [31] for water drops shown in Fig. 8. The drop area is seen to decrease linearly in time, consistent with theory. These tests establish that $a = 1.03$ in

Fig. 7. Comparison of model predictions for centerline trajectories of a gas jet discharging into a cross wind: experimental data for nitrogen by various authors as summarized by Rajaratnam [29]. R is the ratio of discharge velocity to wind speed.

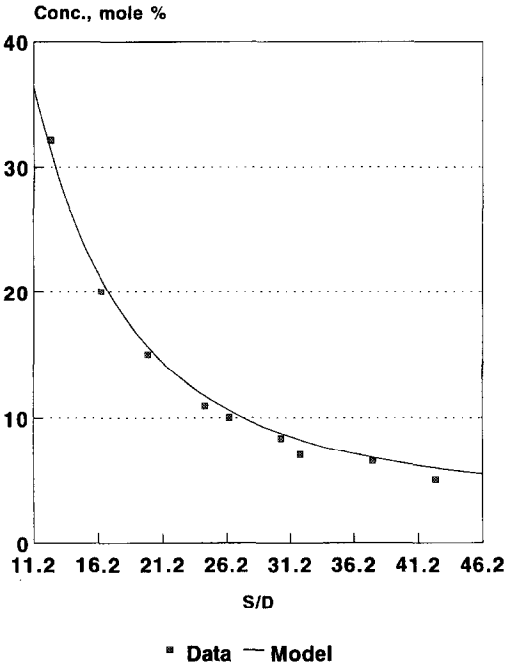

Fig. 6. Comparison of model predictions for centerline concentration of a gas jet of methane in a cross wind: methane discharging at 75 m s^{-1} into a cross wind of 5 m s^{-1}, data by Birch as cited by Cleaver and Edwards [28].

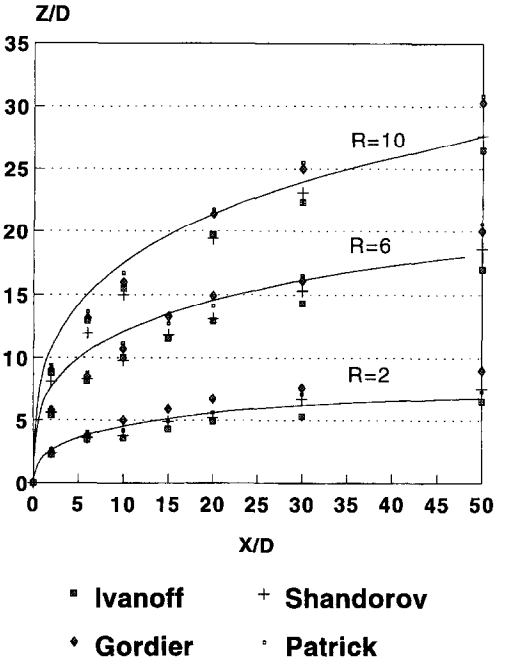

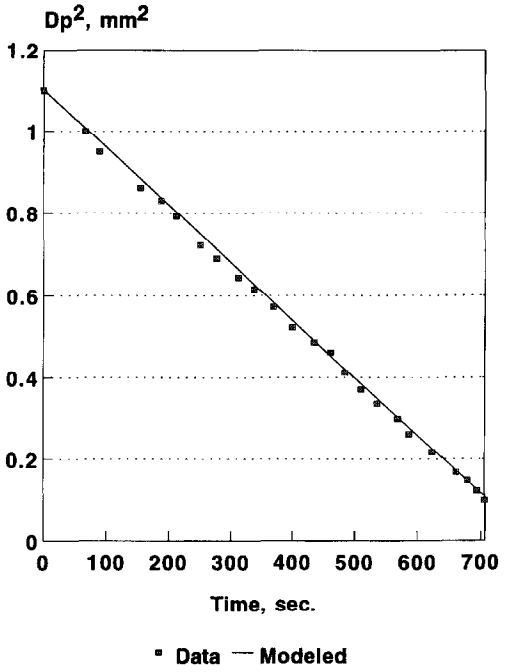

Fig. 8. Comparison of model predictions for evaporation of a single drop of water in still air: experimental data by Ranz and Marshall [31].

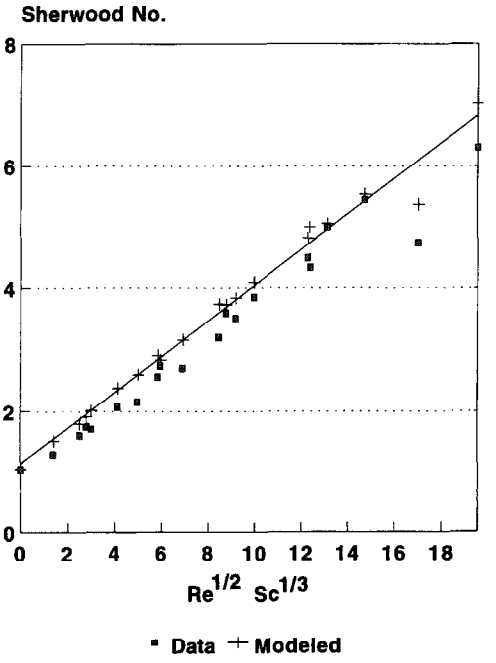

Fig. 9. Comparison of Sherwood number correlation in model with experimental values for benzene and water evaporating in air: experimental data of Ranz and Marshall [31].

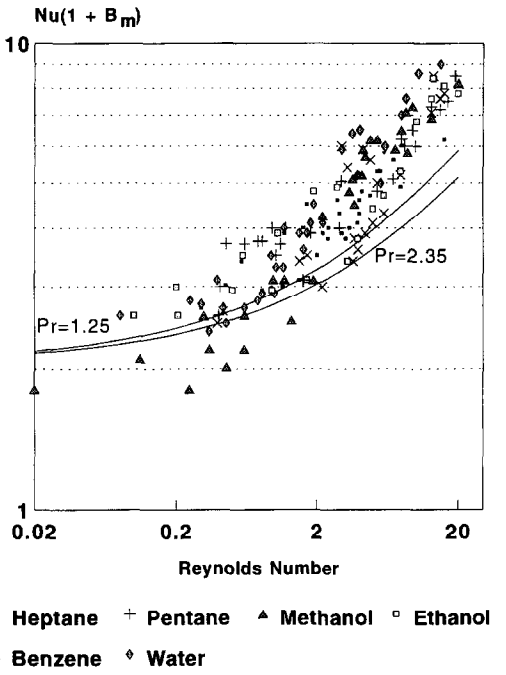

Fig. 10. Comparison of Nusselt number correlation in model with experimental values found by various investigators: experimental data summarized by Eisenklam et al. [12].

Eqs. (21) and (22) to match the water data exactly. That is, the diffusivity reported in the literature and used in our model is within 3% of the value needed to fit Ranz and Marshall's test data. Consequently, we take $a = 1.0$, and accept an error in diffusivity of around ± 3–5%.

– Use single droplet evaporation experiments with constant wind speeds and ambient temperature to set $b = 0.32$ in Eqs. (18) and (19). This is larger than the value of 0.276 given by Fuchs [11], but $0.32/(1 + B_m)$ is near 0.276 for Ranz and Marshall's water and benzene data shown in Fig. 9. This is confirmed against a much larger body of data cited by Eisenklam et al. [12] shown in Fig. 10. Our correlation is accurate at low Reynolds number but is slightly low at high Reynolds number.

– Use standard correlations for deformable drops for C_{Dd}, the droplet drag coefficient.

7. Rainout prediction sensitivities

Figs. 11 and 12 illustrate the sensitivity of UDM rainout predictions to three of the more important variables, drop size, wind speed, and the initial velocity of the drops. At high wind speed, Fig. 11 shows that predicted rainout for water forms an S-shaped curve which is typical of volatile materials. At low wind speed, the relatively non-volatile water droplets approach equilibrium and evaporate slowly, so the rainout

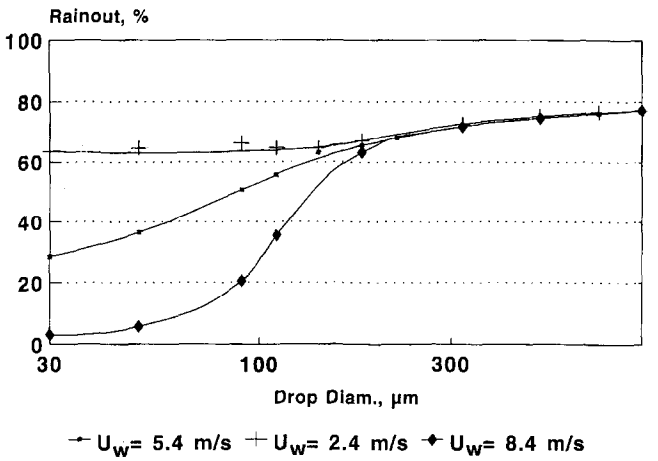

Fig. 11. Sensitivity of UDM predictions of water rainout to wind speed.

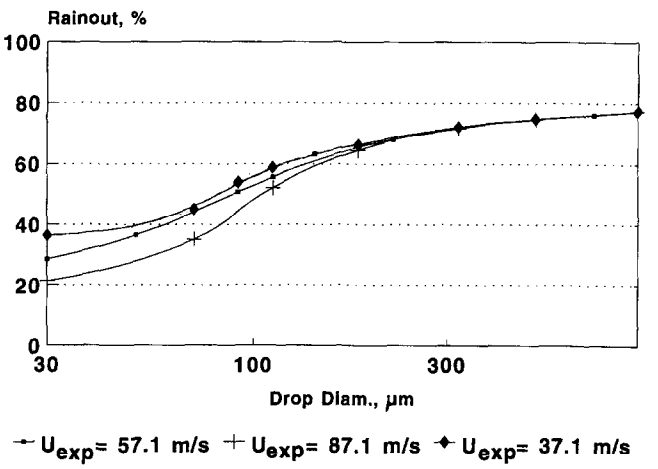

Fig. 12. Sensitivity of water rainout predictions by UDM to expansion velocity.

fraction is less sensitive to drop size. Fig. 12 illustrates that increasing the initial drop velocity (the expansion velocity of the jet) decreases the predicted rainout fraction at smaller drop sizes by increasing the residence time in flight, or the time for the drops to evaporate.

8. Conclusions

A modular, integrated model is described here which makes use of a minimal number of tunable coefficients. A largely decoupled tuning process was used to set the

few constants which can be legitimately adjusted. The resulting match of model predictions with observed data is shown to be good to excellent. Furthermore, predictions match observations well also for experiments in which phenomena are coupled, such as with the spreading and evaporating of volatile materials.

Appendix: Model of pool spread and evaporation

The liquid raining out is modeled as a spreading, circular pool until it reaches the constraints of the edges of the capture pan, or until it reaches a steady-state pool size in which the rate of evaporation and dissolution matches the rate of inflow of mass to the pool. The pool spread rate on a solid substrate is found by numerically integrating the equation given by Opschoor [35].

$$\frac{\mathrm{d}r}{\mathrm{d}t} = [2g(h - h_{\min})]^{1/2}. \tag{A.1}$$

The only adjustable parameter is the minimum pool thickness, $h_{\min}$.

For pools on water, a three regime model is used. Each regime is dominated by the balance of two of the following four forces:

Gravity spreading force:

$$F_G = \pi r^2 h \rho_L \left(\frac{gh\Delta}{r}\right). \tag{A.2}$$

Inertial force:

$$F_I = -\pi r^2 h \rho_L \frac{\mathrm{d}^2 r}{\mathrm{d}t^2} \simeq \pi r^2 h \rho_L \frac{r}{2t^2}. \tag{A.3}$$

Viscous drag force:

$$F_D = \pi r^2 \mu_W \left(\frac{r}{t}\right)\left(\frac{\rho_W}{\mu_W t}\right)^{1/2}. \tag{A.4}$$

Surface tension force:

$$F_S = 2\pi r\sigma. \tag{A.5}$$

The first regime to occur is the gravity–inertia regime when the gravity spreading and inertial forces are approximately equal. This is followed by the gravity–viscous regime when the gravity spreading and viscous drag forces are approximately equal. For involatile liquids which may spread to form thin slicks there may then be a third regime, the viscous–surface tension regime, where the viscous drag and surface tension forces are approximately equal.

Time-explicit analytical solutions and values for four constants are used as reported by Dodge et al. [22]. The heat balance to the pool is:

$$Q_{net} = Q_{cond} + Q_{conv} + Q_{rad} + Q_{sol} + Q_{leak} - Q_{evap}, \tag{A.6}$$

where Q_{cond} is the heat flow rate from conduction (W), Q_{conv} is the heat flow rate from convection (W), Q_{rad} is the heat flow rate from solar radiation (W), Q_{sol} is the heat flow rate from dissolution (W), Q_{leak} is the heat flow rate from leaking liquid (W), and Q_{evap} is the heat flow rate from evaporation (W).

The rate of change of pool temperature may be calculated from the net rate of heat flow into the pool:

$$\frac{dT_{pool}}{dt} = \frac{Q_{net}}{mC_{PL}(T_{pool})}. \tag{A.7}$$

This equation is integrated to obtain the pool temperature as a function of time, with the constraint that it cannot exceed the boiling point of the liquid. If the pool temperature is equal to the boiling point of the liquid then the pool is assumed to be boiling with a rate of heat input given by

$$Q_{boil} = Q_{cond} + Q_{conv} + Q_{rad} + Q_{sol} + Q_{leak} \tag{A.9}$$

resulting in a vaporization rate of

$$\left(\frac{dm}{dt}\right)_{vap} = \frac{Q_{boil}}{h_{fg}}. \tag{A.9}$$

Otherwise, if the pool temperature is below the boiling point then the pool is assumed to be evaporating at that temperature at a rate of

$$\left(\frac{dm}{dt}\right)_{vap} = \frac{Q_{evap}}{h_{fg}}. \tag{A.10}$$

Heat convection from the air to the pool is given by

$$Q_{conv} = k_{air} Nu \frac{\pi r^2}{L}(T_{atm} - T_{pool}). \tag{A.11}$$

The boundary layer is assumed to be laminar for a Reynolds number less than 320 000, and turbulent for higher values. The Nusselt number is then given by

$$Nu = \begin{cases} 0.664 Pr^{1/3} Re^{1/2} & Re < 320\,000, \\ 0.037 Pr^{1/3}[Re^{0.8} - 15200] & Re > 320\,000. \end{cases} \tag{A.12}$$

Evaporation of cyclohexane from the capture pans is modeled by

$$Q_{evap} = 2.10 \times 10^{-3} \pi Sc^{-0.67} u_w^{0.78} r^{1.89} h_{fg} \frac{MWP_a}{RT_{pool}} \ln\left(\frac{P_a}{P_a - P_{sat}}\right), \tag{A.13}$$

which is based upon experimental work of MacKay and Matsugu [23] and Kawamura and MacKay [24], and modified to have a logarithmic driving force by Opschoor [35].

For the chlorine and methylamine cases, a dynamic equilibrium develops between the rate of evaporation and the rate of solution. Evaporation of pools on water is

given by Dodge et al. [22] based on a correlation with the boundary layer Dalton number correlated by

$$Da^* = \left[\frac{Sc_t \log(\delta_+)}{\kappa} + \beta + 2.35\right]^{-1}. \tag{A.14}$$

Using the dimensionless boundary layer thickness given by

$$\delta_+ = \frac{10 u_a^* \rho_{air}}{\mu_{atm}}. \tag{A.16}$$

The Von Karman number κ is set to 0.4 and the turbulent Schmidt number Sc_t to 0.85. The term β is a function of Sc_t and k_v as well as of the Schmidt number, Sc, and a dimensionless wave height, h_w, given by

$$h_W = 0.01384 \frac{u_w u_a^* \rho_{air}}{\mu_{atm}}. \tag{A.16}$$

This then gives a heat loss rate from evaporation of

$$Q_{evap} = \pi r^2 u_a^* Da^* h_{fg} \frac{MWP_a}{RT_{pool}} \ln\left(\frac{P_a}{P_a - P_{sat}}\right). \tag{A.17}$$

Other terms in the heat balance are found with standard methods, as documented in a CCPS report [4].

Nomenclature

a	coefficient, dimensionless
a_2	λW for concentration profiles, W for velocity profiles
a_3	λR for concentration profiles, R for velocity profiles
A_d	droplet surface area, m^2
b	coefficient, dimensionless
B_m	transfer number, $C_{pm}(T_g - T_d)/h_{fg}$
c	concentration, kg of component m^{-3}
c_o	centerline concentration, kg of component m^{-3}
C_D	drag coefficient of drop, dimensionless
C_{Dj}	drag coefficient of plume in air, dimensionless
C_f	friction coefficient, a function of wind speed
C'	correction factor for Stefan flow and the temperature gradient on diffusivity.
C_{pv}	vapor heat capacity of condensable component, $J\,kg^{-1}\,K^{-1}$
C_{pL}	liquid heat capacity of condensable component, $J\,kg^{-1}\,K^{-1}$
C_s	correction for Stefan flow
C_T	correction for the temperature gradient on diffusivity
d_p	droplet diameter, m

D_{12} diffusivity of condensable component in air, $m^2 s^{-1}$
Da^* boundary layer Dalton number
E_{hvy} dense gas entrainment rate, $kg s^{-1}$
E_{jet} high momentum entrainment rate, $kg s^{-1}$
E_{pas} passive dispersion entrainment rate, $kg s^{-1}$
F_h horizontal distribution function, dimensionless
F_v vertical distribution function, dimensionless
g gravitational acceleration, $m s^{-2}$
h heat transfer coefficient, $W m^{-2} K^{-1}$ and thickness of pool, m
h_{fg} heat of vaporization, at T_s, $J kg^{-1}$
h_{min} minimum pool thickness for spreading, m
h_w dimensionless wave height
H effective height of plume, m
I_{dz} vertical component of droplet momentum, $m_d u_{dz}$, $kg m s^{-1}$
I_{x2} partial horizontal plume momentum, $kg m s^{-1}$, $I_x - u_w m_{cld}$
I_x horizontal component of plume momentum, $kg m s^{-1}$
I_z vertical component of plume momentum, $kg m s^{-1}$
k thermal conductivity of the gas, $W m^{-1} K^{-1}$
k_{air} thermal conductivity of air, $W m^{-1} k^{-1}$
K_g mass transfer coefficient, $kg m^{-2} s^{-2}$
L length (diameter) of pool, m
m exponent on distribution functions, dimensionless
m_{cld} mass in plume (instantaneous release) or mass rate in plume (continuous release), kg
m_d droplet mass, kg
MW molecular weight, $kg kmol^{-1}$
Nu Nusselt Number, hr_d/k, dimensionless
P_a ambient pressure, Pa
P_{sat} vapor pressure, Pa
P_{abov} perimeter length of jet, m
Pr Prandtl number, $C_{pm} v_m/k$
q_{GND} heat conduction flux from the ground, $W m^{-2}$
q_F heat conduction by turbulent flow, $W m^{-2}$
q_N heat conduction by natural convection, $W m^{-2}$
r pool radius, m
r_d drop radius, m
R effective radius of plume, m
Re Reynolds number based on the relative velocity of the drops or based on wind speed above pool
S area of cloud in contact with the ground, m^2
Sc Schmidt number, v_m/D_{12}
Sh Sherwood number, $K_g r_d/D_{12}$
s distance along centerline of plume, m or coefficient in power-law profile
t time, s
T_{atm} ambient temperature, K

T_g	temperature of gas phase, K
T_d	temperature of drops, K
T_{pool}	pool temperature, K
u_a^*	friction velocity for air = $u_w (1/2C_f)^{1/2}$
u_d	drop velocity, m s^{-1}
u_o	centerline velocity in plume, m s^{-1}
u_{dg}	relative velocity between drops and jet, $(u_{dgx}^2 + u_{dgz}^2)^{1/2}$, m s^{-1}
u_{dgz}	horizontal component of relative velocity, $u_o \sin\theta - u_d \sin\theta_d$, m s^{-1}
u_{dz}	vertical component of drop velocity, m s^{-1}
u_w	wind speed, m s^{-1}
u_x	$u_{cld} \cos\theta$, horizontal component of cloud velocity, m s^{-1}
u_z	$u_{cld} \sin\theta$, vertical component of cloud velocity, m s^{-1}
W	effective half width of plume, m
x	horizontal distance of cloud centerline, m
x_d	horizontal distance of drops, m
y	crosswind distance of cloud centerline, m
y_g	mole fraction of condensable component in the gas phase around the droplets
y_s	mole fraction of condensable component on the droplet surface, $y_s = P_{sat}(T_d)/P_a$
z	vertical height of cloud centerline, m
z_d	vertical height of drops, m

Greek letters

α_1, α_2	adjustable parameters for plume air entrainment
β	a function of the Schmidt Number
δ_+	dimensionless boundary layer thickness
ε	emissivity of pool, dimensionless
Γ	gamma function
μ_w	viscosity of water, Pa s
μ_{atm}	viscosity of air, Pa s
μ	constant, dependant on composition
κ	Von Karman constant, 0.4
ρ_c	vapor density of condensable component at T_g and P_a, kg m^{-3}
ρ_L	liquid density, kg m^{-3}
ρ_g	gas density, kg m^{-3}
ρ_{cld}	density of plume, kg m^{-3}
ρ_{air}	density of ambient air, kg m^{-3}
σ	surface tension, N m^{-1}
σ_r	Stephan–Boltzmann constant, 5.67×10^{-8}, W m^{-2} K^{-4}
ν_m	kinematic viscosity of gas, m^2 s^{-1}
λ	turbulent Schmidt number, $1.4^{1/2}$
θ	angle to horizontal of plume, rad.
θ_d	angle of drop trajectory to horizontal, rad.

References

[1] Center for Chemical Process Safety, Release characteristics of superheated water and CFC-11 liquids, Final Report by Energy Analysts, Norman, OK, 90-03-540, available through AIChE, NY, 1989.
[2] Center for Chemical Process Safety, Release behavior of superheated chlorine, methylamine, and cyclohexane, Final Report by Quest Consultants, Norman, OK, 91-12-6012, available through AIChE, NY, 1991.
[3] D.W. Johnson, Prediction of aerosol formation from the release of pressurized, superheated liquids to the atmosphere, Internat. Conf. and Workshop on Modeling and Mitigating the Consequences of Accidental Releases of Hazardous Materials, New Orleans, LA, AIChE, CCPS, May 20–24, 1991, pp. 1–34.
[4] Center for Chemical Process Safety, Improved aerosol jet model with rainout, absorption, and reevaporation, Final Report by DNV Technica, Inc, Columbus, OH, available through AIChE, NY, February 1995.
[5] UDM Theory Manual, DNV Technica, Temecula, CA, 1993.
[6] J.L. Woodward and A. Papadourakis, Modeling of droplet entrainment and evaporation in a dispersing jet, Proc. Internat. Conf. and Workshop on Modeling and Mitigating the Consequences of Accidental Releases of Hazardous Materials, New Orleans, LA, AIChE, NY, May 20–24, 1991, pp. 147–168.
[7] J.L. Woodward and A. Papadourakis, Modeling of droplet size, evaporation, and rainout in a dispersing aerosol jet, Internat. Conf. and Exhibition on Safety, Health, and Loss Prevention in the Oil, Chemical, and Process Industries, Singapore, February 15–19, 1993.
[8] J. Cook and J.L. Woodward, A new unified model for jet, dense, passive and buoyant dispersion including droplet evaporation and pool modelling, Internat. Conf. and Exhibition on Safety, Health, and Loss Prevention in the Oil, Chemical, and Process Industries, Singapore, February 15–19, 1993.
[9] J.L. Woodward and J. Cook, Modeling of dispersion with seamless transitions in entrainment mechanism, edge profile, and touchdown with the Unified Dispersion Model, AIChE Meeting, Seattle, WA, August 14–19, 1993.
[10] D.M. Webber, S.J. Jones, G.A. Tickle and T. Wren, A model of a dispersing dense gas cloud and the computer implementation D*R*I*F*T, SRD Reports SRD/HSE R586 and SRD/HSE R587, April 1992.
[11] N.A. Fuchs, Evaporation and Droplet Growth in Gaseous Media, Pergamon Press, Oxford, 1959.
[12] P. Eisenklam, S.A. Arunachalam and J.A. Weston, Evaporation rates and drag resistance of burning drops, 11th Symp. on Combustion at Combustion Institute, Pittsburgh, PA, 1967, pp. 715–728.
[13] R.C. Reid, J.M. Prausnitz and T.K. Sherwood, The Properties of Gases and Liquids, McGraw-Hill, New York, 3rd ed., 1977, p. 555.
[14] J.C. Barrett and C.F. Clement, Growth rates for liquid drops, J. Aerosol Sci., 19 (1988) 223–242.
[15] T. Vesala, J. Kukkonen and M. Kulmala, A model for evaporation of freely falling droplets, Finnish Meteorological Institute Report, Helsinki, 1989, p. 14; also J. Kukkonen, T. Vesala and M. Kulmala, The evaporation of airborne droplets in a turbulent two-phase jet, J Aerosol Sci., 19 (1988) 871–874.
[16] J.L. Woodward, Discharge rates through holes in pipes and process vessels, in: V.M. Fthenakis (Ed.), Prevention and control of accidental releases of hazardous gases, Van Nostrand-Reinhold, New York, 1993, pp. 94–159.
[17] J.L. Woodward, Discharge rates from punctured lines and vessels, in: D.N. Green (Ed.) Perry's Chemical Engineer's Handbook, 7th edn (in print 1995).
[18] R.W. McMullen, J. Air Pollution Control Assoc. Amer., 25 (1975) 1057.
[19] P.R. Hosker, Jr., Estimates of dry deposition and plume depletion over forests and grassland, in: Physical behavior of radioactive contaminants in the atmosphere, Symp. Proc. Internat. Atomic Energy Agency, Vienna, 1973, pp. 291–309.
[20] J.L. Woodward, J. Loss Prev. Process Ind., 3 (1990) 33.
[21] PHAST (Process Hazard Analysis Software Tool) Version 4.2 Release Notes, Appendix I, December 1993.

[22] F.T. Dodge, J.T. Park, J.C. Buckingham and R.J. Magott, Revision and experimental verification of the hazard assessment computer system models for spreading, movement, dissolution, and dissipation of [in]soluble chemicals spilled onto water, US Coast Guard Report CG-D-35-83, Southwest Research Institute, June 1983.
[23] D. MacKay and R. Matsugu, Can. J. Chem. Eng., 51 (1973) 434.
[24] P.I. Kawamura and D. MacKay, The evaporation of volatile liquids, Report to Environment Canada, 1985; J. Hazard Mater., 15 (1987) 343.
[25] E.C. Norman and H.A. Dowell, Using aqueous foams to lessen vaporization from hazardous chemical spills, in: Loss Prevention, Vol. 13, AIChE, New York, 1980.
[26] J.L. Woodward and J. Cook, Tuning a complex suite of dispersion models, Internat. Conf. and Workshop on Modeling and Mitigating the Consequences of Accidental Releases of Hazardous Materials, AIChE, CCPS, New Orleans, LA, Sept. 26–29, 1995.
[27] W.R. Keagy and A.E. Weller, Heat Transfer Fluid Mech Inst., 2 (1949) 89.
[28] R.P. Cleaver and P.D. Edwards, J. Loss Prevention, Process Ind., 3 (1990) 91.
[29] N. Rajaratnam, Turbulent Jets, Elsevier Science Publishers, New York, 1976, p. 184.
[30] J.F. Keffer and W.D. Baines, The round turbulent jet in a cross-wind, J. Fluid Mech., 8 (1963) 481.
[31] W.E. Ranz and W.R. Marshall Jr., Evaporation from drops, Chem. Eng. Prog., 48 (1952) 141, 173.
[32] R. Belore and E. McBean, Modeling the spreading, infiltration, and evaporation of chemical spills on grass and impermeable surfaces, Report EE-86 to Environment Canada, Ontario, Oct. 1986.
[33] R.C. Reid and K.A. Smith, Behavior of LPG on water, Hydrocarbon Processing, (1978) 117–121.
[34] R.C. Reid and K.A. Smith, Confined boiling rates of liquefied petroleum gas on water, EE-77-S-02-4548 MIT, May, 1978.
[35] G. Opschoor, in: Methods for the Calculation of the Physical Effects of Escape of Dangerous Material, TNO Rijswijk, The Netherlands, 1980.